

{001} loops in silicon unraveled

Luis A. Marqués, María Aboy, Manuel Ruiz, Iván Santos, Pedro López, and Lourdes Pelaz.*

Departamento de Electricidad y Electrónica, Universidad de Valladolid, E.T.S.I. de
Telecomunicación, 47011 Valladolid, SPAIN

ABSTRACT: By using classical molecular dynamics simulations and a novel technique to identify defects based on the calculation of atomic strain, we have elucidated the detailed mechanisms leading to the anomalous generation and growth of {001} loops found after ultra-fast laser annealing of ion-implanted Si. We show that the building block of the {001} loops is the very stable Arai tetra-interstitial [N. Arai, S. Takeda, M. Kohyama, Phys. Rev. Lett. 78, 4265 (1997)], but their growth is kinetically prevented within conventional Ostwald ripening mechanisms under standard processing conditions. However, our simulations predict that at temperatures close to the Si melting point, Arai tetra-interstitials directly nucleate at the boundaries of fast diffusing self-interstitial agglomerates, which merge by a coalescence mechanism reaching large sizes in the nanosecond timescale. We demonstrate that the crystallization of such agglomerates into {001} loops and their subsequent growth is mediated by the tensile and compressive strain fields that develop concurrently around the loops. We also show that further annealing produces the unfauling of {001} loops into perfect dislocations. Besides, from the simulations we have fully characterized the {001} loops, determining their atomic structure, interstitial density and formation energy.

KEYWORDS: Silicon, Molecular dynamics, Defects, Laser treatment.

1. Introduction

Silicon is one of the most technologically relevant materials today. For decades, its economical relevance has stimulated a detailed study of its physical properties, especially those related to device processing [1,2]. The understanding of defects has been, and still is, an area of intensive research because of the interesting material science involved and because their presence impacts device performance in many aspects. For example, they have a significant role on the power consumption of integrated circuits (since they induce leakage currents) [3,4], and in the energy conversion efficiency in solar cells (they act as carrier traps) [5]. In particular, due to the influence they have on doping, the study of self-interstitial (\mathcal{S}) defects has driven extensive experimental [6-11] and theoretical [12-18] work, aimed at determining both the structure and properties of such defects and their interaction with dopants. It is well known that dopant implantation generates a large \mathcal{S} supersaturation, and that such excess \mathcal{S} s tend to aggregate in defect clusters of different morphology depending on the particular implant and annealing conditions [11]. For low thermal budgets (short anneals and low temperatures) small \mathcal{S} -clusters are evidenced through spectroscopic techniques [10]. With further anneal, such small clusters grow into the so-called extended defects (EDs) [9,10], which at sizes of several hundred \mathcal{S} s become visible in high-resolution transmission electron microscopy (HRTEM) images [6,11,19]. They show regular atomic structures: frequently EDs form well characterized $\langle 011 \rangle$ \mathcal{S} -chains along $\{113\}$ habit planes (known as $\{113\}$ defects), although for large \mathcal{S} supersaturations and high thermal budgets they adopt the morphology of $\{111\}$ dislocation loops. There are experimental [7,20] and theoretical [21] evidences that $\{111\}$ dislocations are spontaneously generated from the structural transformation of $\{113\}$ defects at such conditions. In parallel with Si vertiginous technology development, defect growth models have been refined to complain with a more detailed prediction

that could guide processing optimization [14]. The Ostwald ripening (OR) mechanism is behind the current understanding of the formation of {113} and {111} EDs in Si. OR implies that EDs are immobile, and that larger and more stable EDs grow by capturing mobile point defects emitted from smaller and less stable EDs [22].

Ultra-fast laser annealing techniques are being explored as a way to achieve high dopant activation with minimal diffusion in ion implanted junctions, without affecting underlying buried layers in 3D integrated devices [23,24]. These techniques are opening a new window of processing conditions, where localized zones of the Si substrate are heated at temperatures close to the melting point for just tens of nanoseconds. In such extreme conditions, planar {001} \mathcal{S} -loops have been observed by HRTEM for the first time in Si [25]. In spite of the short duration of the laser pulse, under 200 ns, a density of the order of $1 \times 10^{11} \text{ cm}^{-2}$ of {001} loops appears. The apparent diameter of the loops was up to 10 nm. Assuming a density of \mathcal{S} s in {001} loops equal to the atomic density of atoms in the Si lattice {001} plane, 13.6 nm^{-2} (to be discussed later), observed {001} loops contain hundreds of \mathcal{S} s. While {001} EDs have been observed in diamond and Ge in the past [19], this particular defect morphology had not been found in Si before, and it was not expected to occur from a thermodynamic point of view, since free formation energy of {001} loops is higher than the corresponding to {111} dislocations [25]. The generation of large {001} loops is not expected either from a kinetic point of view. Within the conventional OR mechanism, the growth of \mathcal{S} -clusters involves the emission and capture of single- \mathcal{S} s. The emission rate ν of single- \mathcal{S} s from \mathcal{S} -clusters with a formation energy E_f is estimated by the expression [26]:

$$\nu = \nu_0 \exp\left(\frac{E_f - E_{f,I} - E_{m,I}}{k_B T}\right)$$

where $E_{f,I}$ and $E_{m,I}$ are the formation and migration energies of the single- \mathcal{S} , respectively, and ν_0 the vibrational frequency of Si atoms ($\sim 10^{13} \text{ s}^{-1}$). Considering $E_{f,I} + E_{m,I} = 4.8 \text{ eV}$ [27] and $E_f \sim 0.6$

eV for a $\{001\}$ loop containing hundreds of \mathcal{S} s [28], even at elevated temperatures close to the Si melting point, the characteristic time for the ripening of large loops ($t = 1/\nu$) is of the order of seconds. This means that conventional OR models are not able to justify the formation of such large $\{001\}$ defects in a nanosecond timescale.

In a recent letter [29], it has been shown that at such elevated temperatures, \mathcal{S} -rich Si is driven into dense liquid-like droplets that are highly mobile within the solid crystalline Si matrix. These liquid droplets merge by a *coalescence* mechanism and eventually transform into $\{001\}$ loops through a liquid-to-solid phase transition in the nanosecond timescale. Although a plausible explanation for the anomalous generation of $\{001\}$ loops has been proposed, some important questions remain unanswered, mainly related to their structural and energetic characterization, and to the microstructural evolution leading to their formation and growth. Sizes and time scales involved in the generation of $\{001\}$ loops make it very difficult the direct experimental determination of such information. In turn, atomistic simulations are very useful for the study of systems at the nano-scale. In particular, the excellent agreement between simulated and experimentally observed atomic structures for other EDs in Si has provided strong evidence for the robustness of the molecular dynamics (MD) technique for defect characterization [30]. Consequently, in this work we use classical MD simulations to unravel the detailed atomistic mechanisms leading to the formation and further growth of $\{001\}$ loops, and to understand the reason for the prevalence of other defect morphologies under conventional annealing conditions. From the simulations we determine the atomic structure of $\{001\}$ loops, their formation energy and \mathcal{S} density. We also show the unfaulting mechanism into perfect $\{001\}$ dislocations.

2. Simulations setup

We have performed our simulations using the open-source MD software package LAMMPS [31]. We have used the Tersoff 3 potential to calculate forces among the Si atoms [32]. It describes the strength of a given bond between two Si atoms as a function of the particular arrangement of other atoms around the bond. This allows correctly describing structures different from perfect crystal, as it is the case of intrinsic defects and the amorphous and liquid phases [30,33]. Besides, Tersoff 3 is able to predict the formation of $\{113\}$ defect precursors at low annealing temperatures in agreement with experiments [17], as we will show later. Nevertheless, Tersoff 3 potential overestimates the Si melting point (2400 K instead of 1685 K [34]). In order to compare simulated Tersoff 3 temperatures T_{T3} with real temperatures T_{real} , it is of common use in the MD community to define a reduced temperature T^* by scaling with respect to melting temperatures:

$$T^* = T_{T3}/2400 = T_{real}/1685$$

We used a quasi-cubic simulation volume filled with a perfect Si lattice composed of $29 \times 42 \times 42$ orthorhombic unit cells, with the X, Y and Z axes lying along the $[100]$, $[011]$ and $[0\bar{1}1]$ directions, respectively. Si lattice parameter was expanded at each simulated temperature according to the Tersoff 3 potential to assure that external pressure in the system is zero. We applied periodic boundary conditions in all directions. We introduced 0.5% of excess \mathcal{S} atoms in tetrahedral positions chosen at random, for a total number of 205647 atoms within the simulation volume. Samples with excess \mathcal{S} atoms were annealed at reduced temperatures T^* ranging from 0.50 to 0.88 (corresponding to real temperatures between 800 K and 1500 K). Simulations are run until a metastable state where all fast moving particles are trapped in immobile stable defects is reached.

A common technique used to identify defects in MD simulations consists of detecting atoms that have displaced from perfect lattice positions a given distance, typically chosen between 0.2

and 0.7 Å [17,35]. However, this method is sensitive to the particular distance used to consider an atom displaced from its lattice site, and it gives no information about the driving force behind the formation and growth of defects. In this work, we use a novel technique to identify defects based on the “effective strain”. It has been shown that defects create strain fields around them, and that such fields affect the interacting elastic energy of surrounding point defects, thus modifying its dynamic behavior [36]. In our simulations, we have calculated the effective strain S (in %) for every atom in the cell, as in the following equation:

$$S = \frac{\sum_{i=1}^n (d_i - d_0)}{nd_0} \times 100$$

where the sum is carried over the first neighbors i of the atom, n is the total number of neighbors, d_i is the distance to neighbor i , and d_0 is the equilibrium distance in the perfect crystal at the simulated temperature. Prior to the calculation of S , we carried time averages of atom coordinates for 1000 time-steps, and subsequent energy minimizations using the steepest descent method. In this way, we filtered out the noise in the values of S due to thermal vibrations [35]. Atoms in the perfect lattice will have S values close to 0. Atoms displaced from perfect lattice positions will have S values that significantly differ from 0: negative values of S (shortened bonds) will correspond to atoms under compressive stress, and positive values (elongated bonds) to atoms under tensile stress. As we shall see, this method adequately allows us to identify defects along MD simulations, and it also gives strain-field related information to understand their nucleation and growth mechanisms.

3. Results and discussion

Our simulations show that single- \mathcal{S} s initially introduced in the lattice and early formed di- and tri- \mathcal{S} s diffuse relatively fast (in agreement with observations by other authors [37,38]). When

they interact, they aggregate into larger defects. At the lowest simulated temperature, $T^* = 0.50$, the aggregation process of all small and mobile species (single-, di- and tri- \mathcal{S} s) results in larger and immobile \mathcal{S} -clusters (with size four and above) that adopt regular and ordered atomic structures. Figure 1 shows the final snapshot of the simulation cell after 170 ns annealing at $T^* = 0.50$. For the sake of clarity, atoms in perfect lattice positions (with S values close to 0) are not shown. A total of 150 different defects are formed with a relatively small \mathcal{S} content (most defects have less than 15 \mathcal{S} s). A few $\{111\}$ rod-like defects [40] appear, but the majority of \mathcal{S} -defects are in the form of (011) chains, isolated tetra- \mathcal{S} s in the compact Arai configuration [41] or small groups of them. It is well known that (011) chains are the precursors of $\{113\}$ defects [19,30], and large $\{113\}$ defects transform into $\{111\}$ dislocations [7,20,21]. Both type of EDs are the most frequent ones experimentally observed under ion-irradiation of Si annealed at temperatures in this regime [11]. However, the role of the Arai tetra- \mathcal{S} is unclear. Extra atoms in the Arai tetra- \mathcal{S} lie on $\{001\}$ planes (see Fig. 2(f)), and such defects aggregate following these same planes, which indicates that Arai tetra- \mathcal{S} s and their agglomerates could be the precursors of $\{001\}$ loops.

In order to evaluate the role of small (011) chains and compact $\{001\}$ aggregates in the ripening of \mathcal{S} -clusters, we have analyzed their atomic configurations (Fig. 2) and energetics (Fig. 3) [42]. In (011) chains, constituent atoms are four-fold coordinated, and their atomic structure is alike when looked in the $\langle 011 \rangle$ direction for all sizes. Formation energies of (011) chains monotonically decrease with size. During the annealing simulation at $T^* = 0.50$ we have observed that these chains capture free \mathcal{S} s on their sides. Captured \mathcal{S} s diffuse along the $\langle 011 \rangle$ direction through the 7-member rings that surround the defect core, until they get to the defect edges where larger tensile strain can accommodate them. This result is in agreement with parallel-replica dynamics calculations carried by Birner and coworkers [43]. In the case of compact $\{001\}$

aggregates, only in the tri- \mathcal{S} cluster and in the multiple-of-four \mathcal{S} configurations constituent atoms are four-fold coordinated. For intermediate configurations extra \mathcal{S} atoms are not four-fold coordinated and, consequently, they are weakly bound (see for example the case of the penta- \mathcal{S} shown in Fig. 2(g), where the core structure is basically the Arai tetra- \mathcal{S} and the extra \mathcal{S} atom is just orbiting around). This is reflected by the formation energies shown in Fig. 3 for compact $\{001\}$ aggregates, which show local minima at the multiple-of-four configurations, with higher energies associated to intermediate configurations. In fact, at the end of our annealing simulation at $T^* = 0.50$ all the observed compact $\{001\}$ agglomerates are multiple-of-four configurations. The existence of particularly stable configurations is in good agreement with the “magic number” clusters found in the inverse modeling of experimental measurements done by Cowern and coworkers [8].

The population of \mathcal{S} -clusters will be consequently determined by the competition between the growth of (011) chains and compact $\{001\}$ agglomerates. Formation energies of the chain tri- \mathcal{S} of Fig. 2(a) and the compact tri- \mathcal{S} of Fig. 2(e) are very similar, around 2.7 eV/ \mathcal{S} , which indicates that their generation from mobile single- and di- \mathcal{S} s is equally likely. Frequent exchange between these two tri- \mathcal{S} clusters configurations is also observed in our MD simulations. When a compact $\{001\}$ tri- \mathcal{S} captures a free single- \mathcal{S} it rapidly transforms to the Arai tetra- \mathcal{S} (see Fig. 2(f)) with a considerable decrease in the energy per \mathcal{S} atom (both defects have a very similar atomic structure). Although the compact Arai tetra- \mathcal{S} has a much lower formation energy than the chain tetra- \mathcal{S} , at low temperatures the structural transformation from chain to compact is unlikely, since it would involve substantial atomic reordering to overcome an energy barrier of around 0.54 eV [44]. In fact, both types of chain and compact \mathcal{S} -clusters are observed at the end of the annealing simulation at $T^* = 0.50$ (Fig. 1). Isolated Arai tetra- \mathcal{S} s and small agglomerates of them are unlikely to further

grow, because additional \mathcal{S} s are weakly bound and once the initial burst of single- \mathcal{S} s is over, it would be extremely infrequent that any given \mathcal{S} -cluster captures simultaneously four free \mathcal{S} s. This limitation does not hold for the chain \mathcal{S} -clusters, which can grow progressively by capturing single- \mathcal{S} s until they get to a critical size that favors the structural transformation to $\{113\}$ defects.

A similar behavior to the one described above for \mathcal{S} aggregation at $T^* = 0.50$ is also observed at annealing temperatures up to $T^* = 0.75$ (corresponding to real temperatures in the interval 800 – 1300 K). Our simulations plot a comprehensive picture of the current understanding of \mathcal{S} -cluster evolution in this temperature regime within the OR mechanism: (a) experimental HRTEM images show large $\{113\}$ defects and $\{111\}$ dislocations (originated from $\{113\}$ EDs), depending on the particular processing thermal budget, but no $\{001\}$ loops are observed, because agglomerates of compact $\{001\}$ tetra- \mathcal{S} s, although very stable, remain so small that cannot be resolved in HRTEM images [11]; (b) The existence of “magic number” \mathcal{S} -cluster configurations, associated to the multiple-of-four $\{001\}$ Arai defects and demonstrated by Cowern *et al.* [8], is compatible with the growth of chain (011) \mathcal{S} -defects characterized by a formation energy that monotonically decreases with size; and (c) the growth of large $\{001\}$ loops from small Arai agglomerates is kinetically prevented, even though the generation of the former appears to be thermodynamically favorable (their formation energy is lower than the corresponding to $\{113\}$ defects, as we shall see later).

In our simulations, defects resulting after annealing at high temperatures, above $T^* = 0.75$, are fewer, with sizes large enough to be considered as EDs, and they contain a high amount of \mathcal{S} s. Figure 4 shows snapshots corresponding to the final system configurations after annealing at the three higher temperatures considered in this work, $T^* = 0.79$, 0.83 and 0.88 (corresponding to real temperatures between 1300 and 1500 K). Some Arai tetra- \mathcal{S} s remain after annealing at $T^* = 0.79$, but no $\{011\}$ chains are observed at any of these temperatures. Instead, we find large disks of \mathcal{S}

atoms lying on $\{001\}$ planes, which can be consequently identified with planar $\{001\}$ loops. These $\{001\}$ defects coexist with some $\{111\}$ dislocations. From the final configurations shown in Fig. 4 we have extracted the average size of $\{001\}$ defects, their formation energy, the $\{001\}$ EDs density, and the relative amount of \mathcal{S} s belonging to $\{001\}$ and $\{111\}$ EDs. These data are collected in Table 1. Our simulations show that $\{001\}$ loop sizes and the relative percentage of \mathcal{S} s in $\{001\}$ defects with respect to $\{111\}$ dislocations increase with temperature, while $\{001\}$ defects density decreases, in very good agreement with experimental observations [25,45]. Extracted formation energies per \mathcal{S} atom decrease with temperature, because $\{001\}$ loops become larger and the contribution of the interfacial energy diminishes.

In this high temperature regime, the mechanisms for the generation of $\{001\}$ loops appear to be completely different from the conventional OR process: instead of having ordered and immobile \mathcal{S} -defect clusters exchanging mobile point-defect \mathcal{S} s, we observe that \mathcal{S} -clusters remain completely disordered for sizes of tens or even hundreds of \mathcal{S} s. They are of liquid nature, highly mobile and rapidly merge by a coalescence mechanism [29]. Figure 5 shows the measured effective diffusivities as a function of time for all the annealing simulations carried in this work. They have been calculated by applying the Einstein formula that relates diffusivity D at a given time t with the total mean square displacement in the simulation cell:

$$D(t) = \frac{1}{6N_I t} \sum_{i=1}^N |\vec{r}_i(t) - \vec{r}_i(0)|^2$$

where \vec{r}_i is the position vector of atom i , N the total number of atoms in the simulation, and N_I the number of extra \mathcal{S} atoms in the MD cell. For temperatures between $T^* = 0.50$ and $T^* = 0.75$ we see an initial plateau corresponding to the weighted average diffusivity of highly-mobile species (single \mathcal{S} s, di- \mathcal{S} s and tri- \mathcal{S} s), which is of the order of the diffusivity calculated for single- \mathcal{S} s [35].

This initial plateau is followed by a dependence close to $1/t$, indicative of a halted diffusion when mobile \mathcal{S} s become trapped in stable immobile clusters (such as Arai tetra- \mathcal{S} s). At the three higher temperatures, apart from the initial plateau, we notice an additional plateau at intermediate times revealing the onset of other mobile species, i.e., the liquid-like \mathcal{S} -rich clusters. Such dependence turns again into $1/t$ when these disordered clusters transform into immobile planar $\{001\}$ loops. The high diffusivities of these liquid-like \mathcal{S} -rich agglomerates ($\geq 10^{-5}$ cm²/s) imply that they can travel distances of the order of nanometers in a nanosecond timescale. Thus, the merging of highly mobile \mathcal{S} -agglomerates leads to the formation of large \mathcal{S} -clusters within nanoseconds, contrary to OR mechanism that would require times of the order of seconds to exchange single- \mathcal{S} s among stable and immobile \mathcal{S} -clusters. It is worth to note that the density and diameter of $\{001\}$ loops extracted from experiments [25,45] are comparable to the results obtained in our simulations, which give an average distance among $\{001\}$ loops of ~ 10 nm and sizes of hundreds of \mathcal{S} s (values derived from data in Table 1).

Atoms surrounding $\{001\}$ loops, even though they are in perfect lattice positions, appear colored (strained) in Fig. 4. We found that $\{001\}$ loops produce strong strain fields around them, of two different types. One type is associated to atoms above and below the disk of extra \mathcal{S} atoms, colored green, and consequently corresponds with light compressive stress. They define a volume with the shape of an ellipsoid, and it is clearly visible in $\{001\}$ loops viewed from the side (like, for example, defect labeled as “A” in Fig. 4). The other type is associated to atoms that surround the circle defined by the disk of extra \mathcal{S} s. These atoms are displayed with warm colors, from yellow to red, indicating that they are under tensile stress. They define a volume with the shape of a toroid, and it appears as a circumference that surrounds the $\{001\}$ loop in a plain view (for example, in defect labeled as “B” in Fig. 4). Both strain fields are a consequence of the extra \mathcal{S} atoms in the

defect core, which pull outwards the crystal lattice above and below the defect plane compressing the corresponding bonds, and at the same time causing the elongation of bonds around the extra \mathcal{S} -atoms disk. The presence of these strain fields affect the movement of other \mathcal{S} -agglomerates trough the lattice [36]: compressive strain fields increase the elastic interacting energy of \mathcal{S} -defects, while tensile strain fields decrease it; consequently, \mathcal{S} -defects will tend to move out of compressive strain regions and towards tensile strain zones.

Our MD simulations have revealed the detailed atomic mechanisms leading to the generation of $\{001\}$ loops. Figure 6 shows several snapshots taken during annealing at $T^* = 0.83$ depicting the formation of a $\{001\}$ loop. Figure 6(a) displays one of the highly mobile liquid droplets formed during the \mathcal{S} aggregation process. It has a quasi-spherical shape to minimize the surface-to-volume ratio and, consequently, the interfacial free energy. Recrystallization of the liquid droplet starts from the spontaneous nucleation of Arai tetra- \mathcal{S} s at the interface with the crystal lattice. The Arai tetra- \mathcal{S} is the only ordered \mathcal{S} -cluster able to withstand such high temperatures, due to its extraordinarily high vibrational entropy [46,47]. Its particular atomic structure, where all atoms are perfectly four-fold coordinated (see Fig. 2(f)), favors their formation at the interface between the liquid agglomerates and the crystal lattice, naturally accommodating within the crystal the excess \mathcal{S} content of the liquid droplets. Frequently, randomly nucleated Arai tetra- \mathcal{S} s dissolve again into the liquid agglomerates. Only when two Arai tetra- \mathcal{S} s nucleate close together, they become stable enough to withstand thermal agitation (the compact Arai octo- \mathcal{S} cluster is much more stable than two isolated Arai tetra- \mathcal{S} s, due to its lower formation energy, as shown in Fig. 3). The strain field created by the Arai tetra- \mathcal{S} s, shown in the inset Fig. 6, favors that extra \mathcal{S} atoms in the liquid droplet, initially distributed uniformly throughout its volume, concentrate in the $\{001\}$ plane where the extra \mathcal{S} atoms of the Arai defect lie (see Fig. 6(b)). This process, in turn, strengthens the strain

field (compressive above and below, and tensile around), so atoms rapidly redistribute within the droplet into a disk of a circular shape (see Fig. 6(c)). The transformation from a liquid droplet to a fully ordered $\{001\}$ loop occurs in few nanoseconds (Fig. 6(d)), and it can be described as a first-order phase transition [29], which needs the prior nucleation of Arai tetra- \mathcal{S} s (incubation period) that afterwards act as the seed for the droplet crystallization. From our simulations, we have measured a latent heat of $0.42 \text{ eV}/\mathcal{S}$ in the transformation, of the order of the latent heat for melting in Si calculated with the Tersoff 3 potential [48].

$\{001\}$ loops can further grow while still other mobile liquid droplets, containing hundreds of \mathcal{S} s, coexist, as depicted in Fig. 7 corresponding to the annealing simulation at $T^* = 0.79$. The compressive strain field created by the loop above and below the defect plane pulls the approaching mobile liquid \mathcal{S} -cluster to the loop edge, where the strain is tensile and the \mathcal{S} s can be incorporated. Atoms in the liquid droplet start to rearrange following the ordered structure of the loop, via the generation of Arai tetra- \mathcal{S} s, growing in size while maintaining its planar structure. The incorporation of the liquid droplet into the $\{001\}$ loop is very fast, atomic reordering occurs within just 1.4 ns, and it is accompanied by a decrease of the potential energy in the system.

Atomic structures of all $\{001\}$ defects formed in our simulations are similar to the one shown in the snapshots of Fig. 6(d). In the loop edges, atoms are arranged following the structure of the Arai tetra- \mathcal{S} , in alternate positions within the crystal lattice, like in a chessboard. This arrangement is similar to the atomic structure proposed by Takeda for the case of $\{001\}$ defects in Ge [19], which is displayed in Fig. 8(a). However, a closer look into the $\{001\}$ defects obtained in our simulations indicates that atoms arrange differently in the loop cores, as shown in Fig. 8(b). While in Takeda's configuration the typical Arai tetra- \mathcal{S} s structure is maintained, with 8-member atom rings in between, in our structure extra \mathcal{S} atoms distribute uniformly along the defect plane. This

reordering is energetically favorable, since the formation energy per \mathcal{S} atom decreases from 0.74 eV in Takeda's arrangement to 0.68 eV in our structure. Figure 8(c) shows the HRTEM image obtained from Qiu and coworkers of the $\{001\}$ loops found in their experiments [25]. Figures 8(d) and 8(e) show HRTEM simulated images [49] of the atomic structures shown in Fig. 8(a) and 8(b), respectively. As it can be seen, the experimental HRTEM image compares very well with the corresponding to the structure found in our simulations, while the simulated image of Takeda's structure shows large white spots corresponding to the 8-member rings. This indicates that $\{001\}$ EDs in Si adopt a different configuration than in Ge.

From our simulations, we have also characterized in detail this newly found structure. We have measured a Burgers vector of one-third the lattice unit a in the $[001]$ direction, within the experimental error of the $a/4 [001]$ value reported by Qiu and coworkers [25]. In Table 2 we indicate the formation energy E_f per \mathcal{S} atom and the \mathcal{S} density for the $\{001\}$ loops and other common EDs in Si (considered ideal and infinite). In $\{001\}$ loops, the formation energy is slightly higher than that corresponding to the $\{111\}$ rod-like defects, and \mathcal{S} density is high, close to the maximum value typical of perfect $\{111\}$ dislocations. The higher energy of $\{001\}$ loops compared to $\{111\}$ defects made them thermodynamically unexpected.

Since \mathcal{S} density in $\{001\}$ loops coincides with the atomic Si density in $\{001\}$ planes (see Table 2), it is expected that some of the loops will unfault. To study this transformation, we carried out MD simulations with a perfect Si lattice composed of $10 \times 18 \times 10$ orthorhombic unit cells, with the X, Y and Z axes lying along the $[011]$, $[100]$ and $[01\bar{1}]$ directions, respectively. In the center of the cell, and within a plane perpendicular to the Y axis, we introduced 200 extra atoms (for a total of 7400 atoms in the simulation) following the configuration we found for the $\{001\}$ loops. We applied periodic boundary conditions in all directions in order to simulate the behavior of an

infinite $\{001\}$ loop embedded in the crystal lattice. The dimensions of the cell along the Y axis were made longer than in the case of X and Z axes in order to avoid that periodic boundary conditions affect the free movement of atoms in the Y direction. The MD cell was annealed at $T^* = 0.79$ for 4 nanoseconds. Figure 9 shows several snapshots taken during the simulation depicting the $\{001\}$ loop unfauling into a perfect dislocation. Unfauling starts with the spontaneous occurrence of a bond switch in the loop core. This initial event produces a collective and coordinate movement of atoms exchanging their bonds and causing the glide of the crystal planes immediately above the loop, within just a few picoseconds. Finally, the crystal lattice is restored, but $\{001\}$ loop unfauling leaves behind a screw dislocation. The facts that the infinite $\{001\}$ loop remained stable in its initial configuration for 3.6 ns at $T^* = 0.79$ before unfauling, and that in our previous MD simulations of \mathcal{S} aggregation we have not observed this kind of transformation in finite $\{001\}$ loops even after 30 ns of annealing at that temperature (see Fig. 4(a)), indicate that an energy barrier that decreases with defect size must be overcome for unfauling to occur. We have observed that for annealings at $T^* = 0.83$ and $T^* = 0.88$ some of the formed finite $\{001\}$ loops unfault into perfect dislocations (EDs indicated by dark green arrows in Fig. 4(b) and (c)). Larger loop sizes are favored by higher annealing temperatures [29], which in turn stimulate further atomic agitation within the loop cores, making more likely the unfauling transformation.

4. Conclusions

We have used MD simulations to show in detail the atomistic mechanisms related to the formation, growth and unfauling of $\{001\}$ loops recently found in ion-implanted Si after ultra-fast laser annealing treatments. We have shown that the building block of the $\{001\}$ loops is the Arai tetra- \mathcal{S} . At low annealing temperatures (typical of conventional annealing treatments), \mathcal{S}

aggregation proceeds via OR, with ordered and immobile \mathcal{S} -clusters exchanging mobile single-, di- and tri- \mathcal{S} s. In these conditions, the growth of Arai tetra- \mathcal{S} agglomerates ($\{001\}$ loops precursors) is not favored with respect to the ripening of (011) chains ($\{113\}$ defects precursors), given the variation of formation energies of such families of defects as a function of size. We have demonstrated that, at high annealing temperatures (typical of ultra-fast laser annealing treatments), \mathcal{S} -agglomerates exhibit a high diffusivity; they can coalesce in the nanosecond timescale, making it possible the formation of large \mathcal{S} -defects nine orders of magnitude faster than conventional OR would predict. The generation of $\{001\}$ loops also occurs in the nanosecond timescale, starting by the spontaneous nucleation of Arai tetra- \mathcal{S} s at the boundaries of such \mathcal{S} -rich agglomerates. By using a novel technique for defect identification based on the calculation of atomic strain, we have shown that the formation of $\{001\}$ loops, and the subsequent growth of these loops by capturing additional agglomerates, are mediated by the two types of strain fields that build up around the loops: tensile in the loop edges and compressive above and below the defect plane. Finally, with further annealing at the highest temperatures, we found that $\{001\}$ loops unfault into perfect dislocations.

The key for the formation of $\{001\}$ loops is that, under ultra-fast laser annealing conditions, the Si sample is heated at temperatures close to the melting point in the nanosecond timescale, leading to the formation of large \mathcal{S} -rich liquid droplets. The Arai tetra- \mathcal{S} is the only ordered defect structure able to withstand such high temperatures to nucleate at the edges of the droplets and produce their transformation into regular $\{001\}$ loops. This high-temperature regime only lasts for several hundreds of nanoseconds, then temperature drops very fast, so the $\{001\}$ loops become undercooled within the lattice. Under conventional (furnace or flash) annealing, such high temperatures can also be reached, but ramping up, heating, and cooling down last for times orders of magnitude longer than those typical of ultra-fast laser annealing. At lower temperatures (as it

occurs during the “slow” temperature ramp-up), self- \mathcal{S} clusters will evolve according to the OR mechanism, which eventually leads to $\{113\}$ defects and $\{111\}$ dislocation loops. Since $\{111\}$ dislocations are lower in energy than $\{001\}$ defects, once self-interstitials are stored in $\{111\}$ dislocations, $\{001\}$ loop formation is suppressed. This is coherent with the fact that $\{001\}$ loops have not been observed in Si under conventional annealing conditions.

The atomic structure we observe in the core of generated $\{001\}$ loops differs from the one formerly proposed for such defects in Ge by Takeda. The atomic structure we propose is fully consistent with experimental HRTEM images, and it is the result of a comprehensive formation mechanism. From the simulations we have also extracted the formation energy per \mathcal{S} atom (0.68 eV) and the \mathcal{S} density (13.6 nm^{-2}) of $\{001\}$ loops. This information is relevant from a practical point of view, because from the measurable size distribution and \mathcal{S} density of $\{001\}$ loops it is possible to evaluate the total amount of \mathcal{S} s stored in such defects. They are also key parameters for predictive TCAD modeling of ultra-fast laser annealing treatments or other extremely high temperature processing steps.

Acknowledgements

This work has been supported by the European Union (FEDER) and the Spanish Ministerio de Ciencia e Innovación under Project No. TEC2014-60694-P, and by the Junta de Castilla y León Consejería de Educación under Project No. VA119G18.

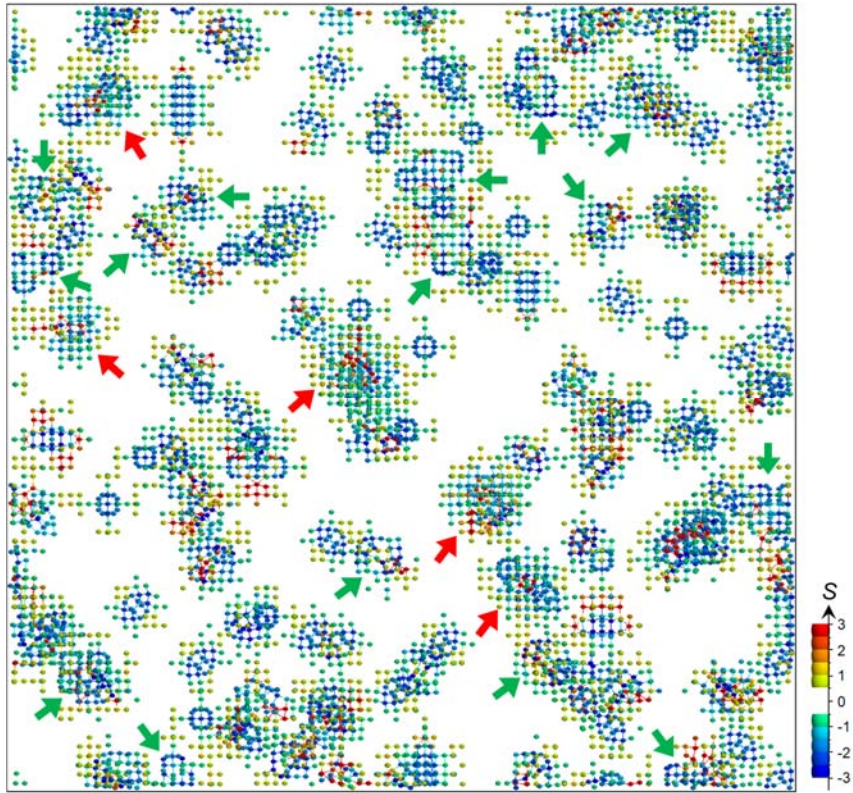


Figure 1. ZY snapshot of the simulation cell after annealing at $T^* = 0.50$ for 170 ns. Atomic colors identify the corresponding S values [39]. $\{111\}$ rod-like defects are indicated by red arrows and agglomerates of Arai tetra- \mathcal{S} s by green arrows. Remaining defects are isolated Arai tetra- \mathcal{S} s and (011) chains.

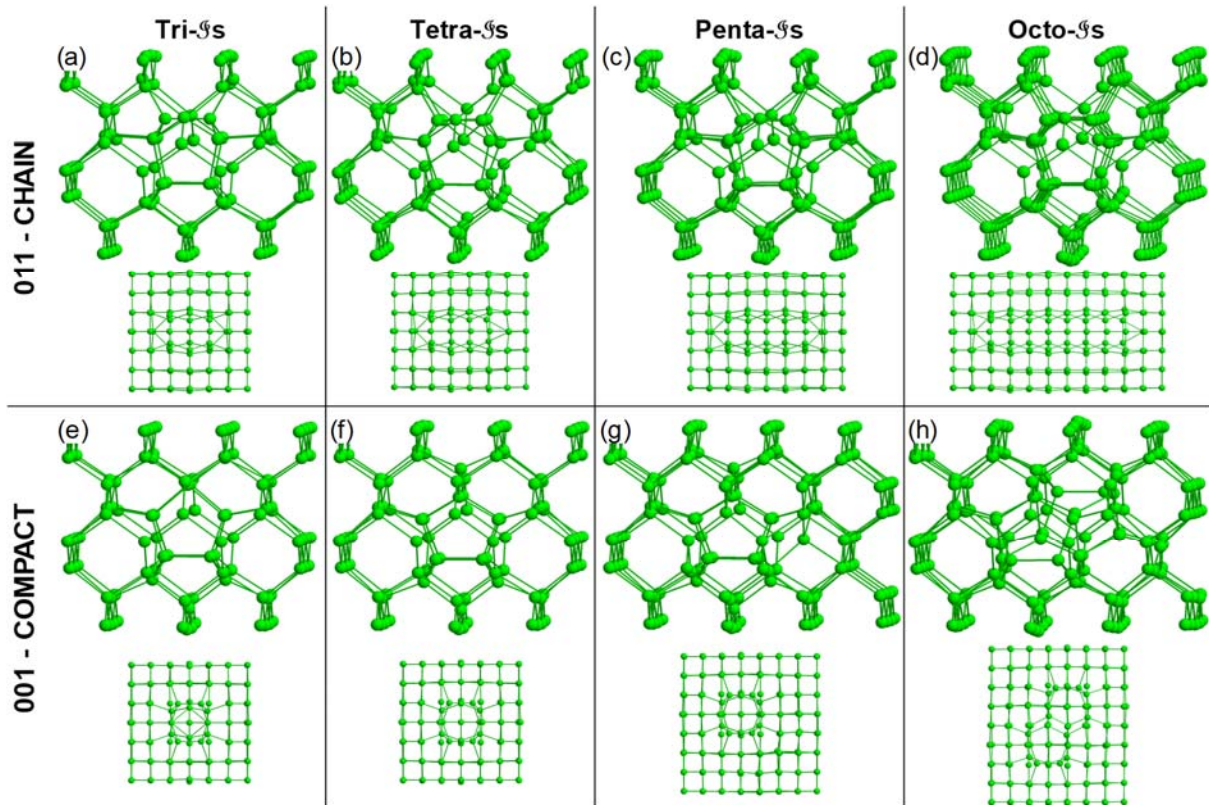


Figure 2. Ball and stick models of chain and compact \mathcal{S} -clusters of 3, 4, 5 and 8 \mathcal{S} s. Below each model, top views of the defects along the $\langle 001 \rangle$ direction, which show the elongated and compact nature of each family of precursors.

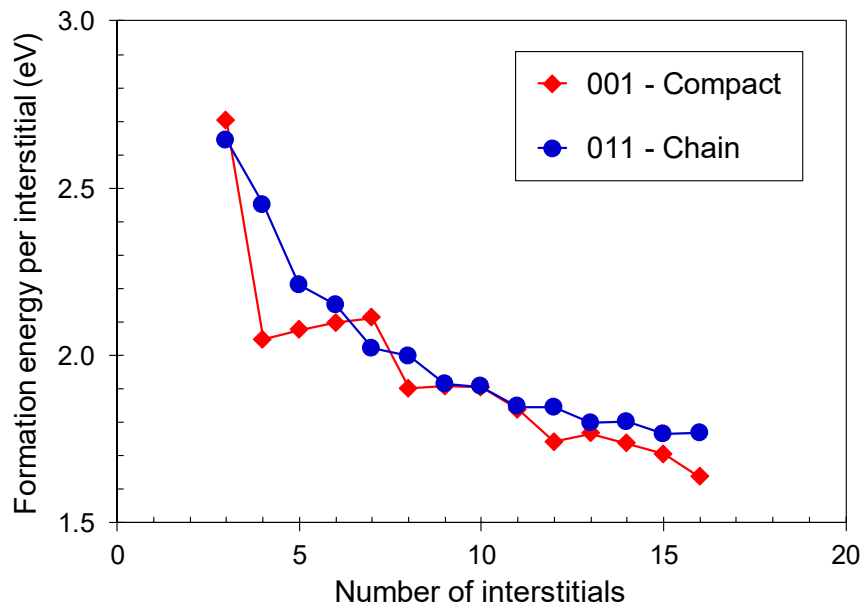


Figure 3. Formation energy per \mathcal{S} atom in chain and compact \mathcal{S} -clusters for sizes 3 to 16.

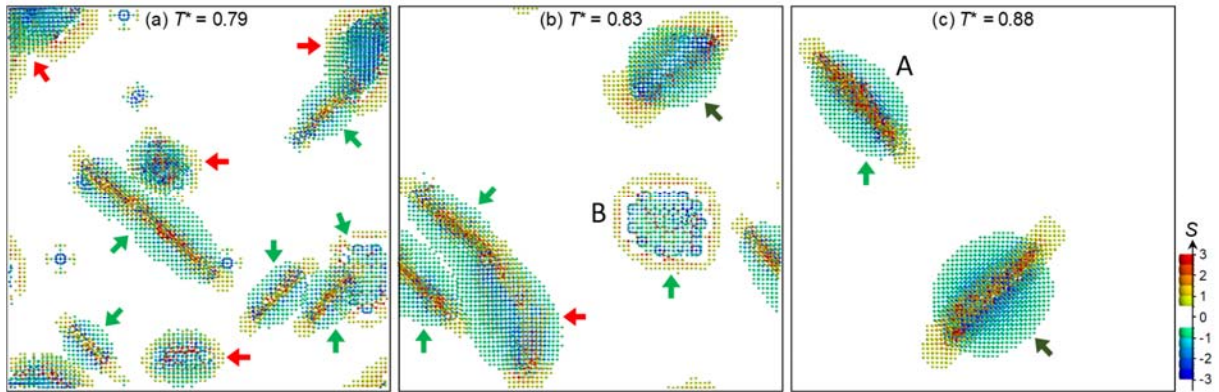


Figure 4. ZY snapshots of the simulation cell after annealing at (a) $T^* = 0.79$ for 30 ns, (b) $T^* = 0.83$ for 29 ns, and (c) $T^* = 0.88$ for 74 ns. Atomic colors identify the corresponding S values [39]. $\{111\}$ dislocations are indicated by red arrows and $\{001\}$ EDs by green arrows (dark green are perfect dislocations, the rest are $\{001\}$ loops). Remaining defects in (a) are isolated Arai tetrahedra. Defects labeled as A and B show how strain fields created by the $\{001\}$ loops look like on side- and plain-views, respectively.

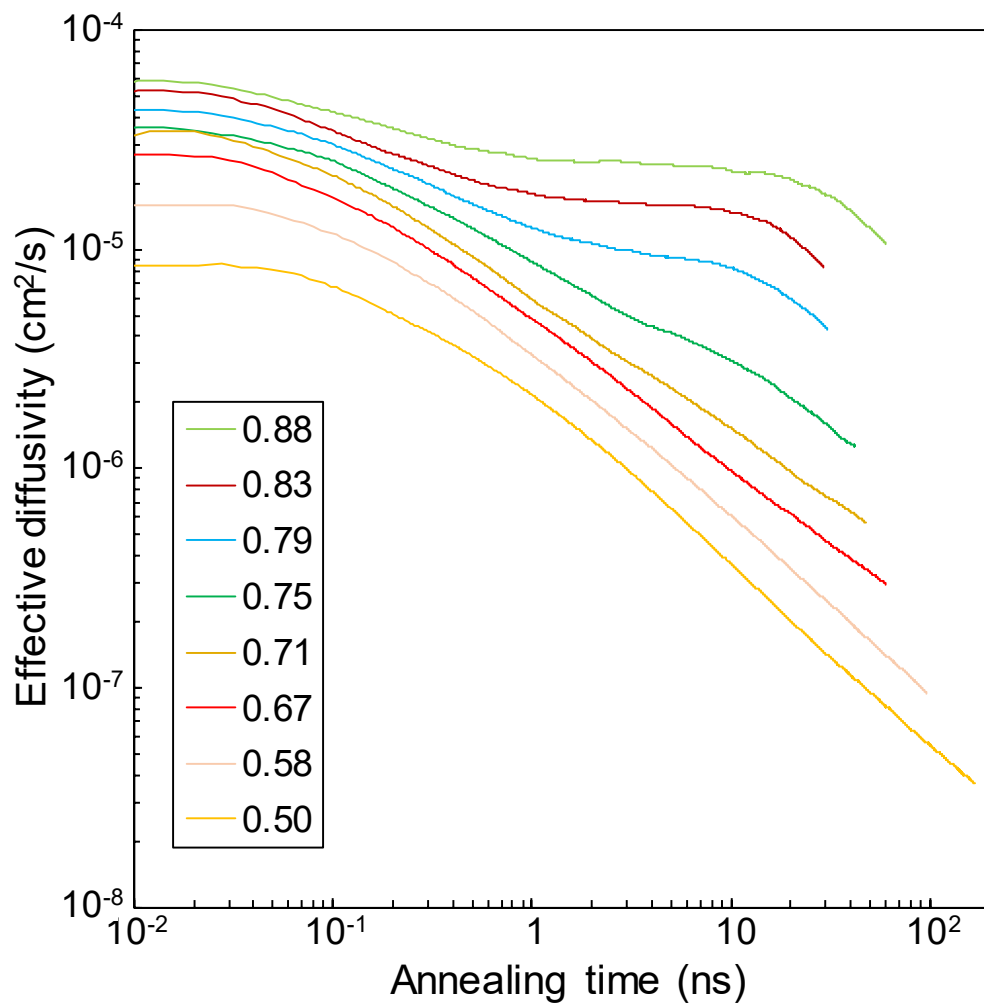


Figure 5. Effective diffusivities as a function of time during annealing at several reduced temperatures.

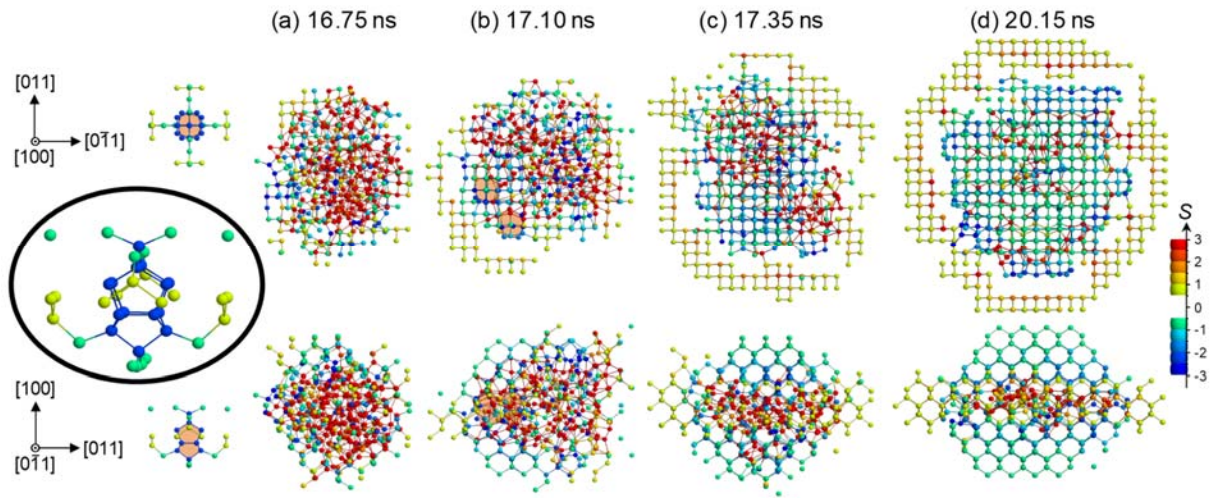


Figure 6. Snapshots depicting the formation of one $\{001\}$ loop from a liquid \mathcal{S} -cluster during annealing at $T^* = 0.83$. Defect contains a total of 100 \mathcal{S} s. Upper snapshots correspond to plain views, and bottom snapshots with side views. Atomic colors identify the corresponding S values [39]. Times are measured from the start of the annealing simulation. On the left, the strain field created by the Arai tetra- \mathcal{S} , shown in perspective and projected along the $\langle 001 \rangle$ and $\langle 011 \rangle$ directions. Around the four extra atoms in the Arai defect the strain field is tensile, while above and below the defect is compressive, which favors close \mathcal{S} s to align on a $\{001\}$ plane. Arai tetra- \mathcal{S} s that nucleate in the liquid \mathcal{S} -cluster edges in (b) are shadowed in red.

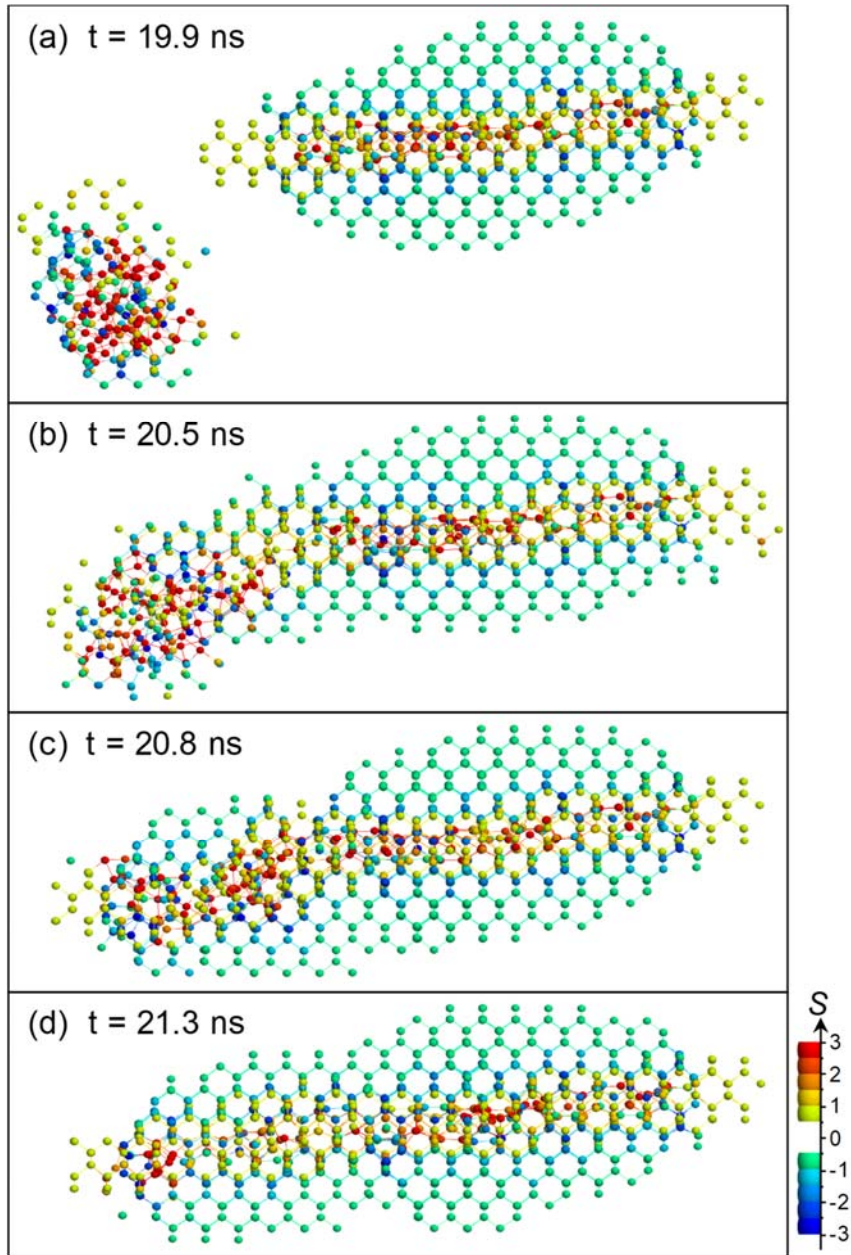


Figure 7. ZY snapshots depicting the growth of one $\{001\}$ loop at the expense of a liquid S -cluster during annealing at $T^* = 0.79$. Atomic colors identify the corresponding S values [39]. Times are measured from the start of the MD simulation.

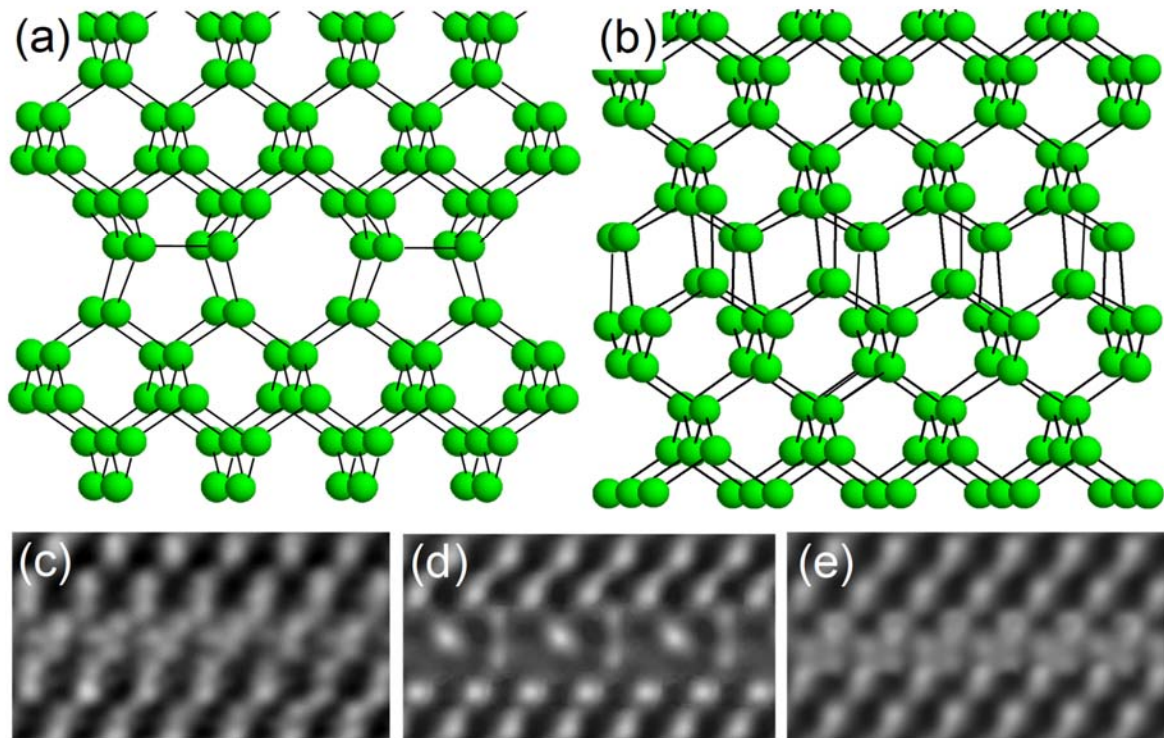


Figure 8. Atomic structure of the $\{001\}$ loops: (a) as proposed by Takeda in Ref. [19], (b) atomic rearrangement observed in our MD simulations, (c) experimental HTREM image from Ref. [25], (d) simulated HRTEM image of the structure shown in (a), and (e) simulated HRTEM image of the structure shown in (b) [49].

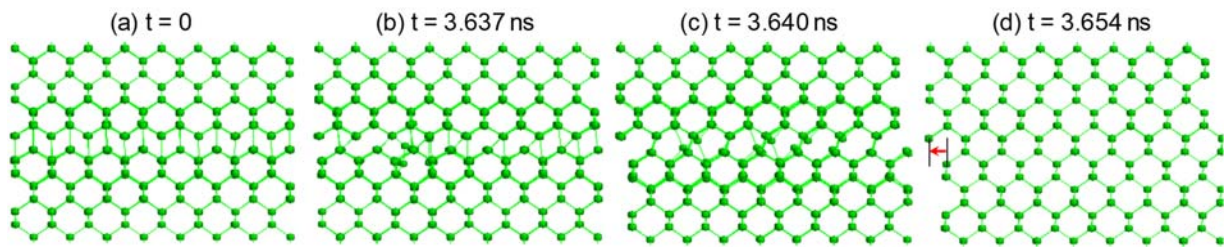


Figure 9. XY snapshots taken during annealing at $T^* = 0.79$ depicting the unfauling of an infinite $\{001\}$ loop (not all the atoms in the MD cell are shown). Times are measured from the start of the MD simulation. Arrow in the last snapshot indicates the resulting edge dislocation.

| T^* | Average size | Formation energy (eV/§) | {001} defects density (cm ⁻³) | % of §s in {001}/{111} EDs |
|-------|--------------|-------------------------|---|----------------------------|
| 0.79 | 100 | 0.89 | 1.46×10^{18} | 57/40 |
| 0.83 | 256 | 0.84 | 9.76×10^{17} | 79/21 |
| 0.88 | 511 | 0.77 | 4.88×10^{17} | 100/0 |

Table 1. Results of the annealing simulations at several reduced temperatures: average sizes of resulting {001} loops, formation energies, defects densities, and percentages of §s in {001} and {111} EDs.

| Extended defect | Atomic structure | E_f per \mathcal{S} atom (eV) | \mathcal{S} density (nm^{-2}) |
|-------------------------------|------------------|-----------------------------------|--|
| $\{113\} \text{IIO} $ | | 0.86 | 5.4 |
| $\{001\}$ loop | | 0.68 | 13.6 |
| $\{111\}$ rod-like defect | | 0.65 | 7.8 |
| $\{001\}$ perfect dislocation | | 0 | 13.6 |
| $\{111\}$ perfect dislocation | | 0 | 15.7 |

Table 2. Features of typical EDs in Si. Atoms in red indicate the extra \mathcal{S} s. Formation energies in the case of ideal and infinite $\{001\}$ and $\{111\}$ dislocations are 0 because atomic arrangements are that of the perfect lattice.

References

* Corresponding author. E-mail: lmарques@ele.uva.es. Tel. +34 983 185503.

- [1] M. Jeong, B. Doris, J. Kedzierski, K. Rim, M. Yang. Silicon device scaling to the sub-10-nm regime, *Science* 306, 2057-2060 (2004).
- [2] W. Bergholz. Defect engineering in silicon materials, in: Y. Yoshida, G. Langouche (eds.) *Defects and impurities in silicon materials. Lecture Notes in Physics*, vol. 916. Springer, Tokyo, 2015.
- [3] R. Duffy, A. Heringa, V.C. Venezia, J. Loo, M.A. Verheijen, M.J.P. Hopstaken, K. van der Tak, M. de Potter, J.C. Hooker, P. Meunier-Beillard, R. Delhougne. Quantitative prediction of junction leakage in bulk-technology CMOS devices, *Solid-State Electron.* 54, 243-251 (2010).
- [4] C.-P. Chou, C.-Y. Chen, K.-Y. Chen, S.-C. Teng, Y.-H. Wu. Improved leakage current and device uniformity for sub-20 nm N-FinFETs by cryogenic Ge pre-amorphization implant in contact, *Microelectron. Eng.* 178, 137-140 (2017).
- [5] M. A. Green, S. P. Bremner. Energy conversion approaches and materials for high-efficiency photovoltaics, *Nature Materials* 16, 23-34 (2017).
- [6] D. J. Eaglesham, P. A. Stolk, H. J. Gossmann, J. M. Poate. Implantation and transient B diffusion in Si: The source of the interstitials, *Appl. Phys. Lett.* 65, 2305-2307 (1994).
- [7] J. Li, K. S. Jones. $\{311\}$ defects in silicon: The source of the loops, *Appl. Phys. Lett.* 73, 3748-3750 (1998).
- [8] N. E. B. Cowern, G. Mannino, P. A. Stolk, F. Roozeboom, H. G. A. Huizing, J. G. M. van Berkum, F. Cristiano, A. Claverie, M. Jaraíz. Energetics of self-interstitial clusters in Si, *Phys. Rev. Lett.* 82, 4460-4463 (1999).

- [9] S. Coffa, S. Libertino, C. Spinella. Transition from small interstitial clusters to extended $\{311\}$ defects in ion-implanted Si, *Appl. Phys. Lett.* 76, 321-323 (2000).
- [10] S. Libertino, S. Coffa, J. L. Benton. Formation, evolution, and annihilation of interstitial clusters in ion-implanted Si, *Phys. Rev. B* 63, 195206 (2001).
- [11] A. Claverie, B. Colombeau, B. de Mauduit, C. Bonafos, X. Hebras, G. Ben Assayag, F. Cristiano. Extended defects in shallow implants, *Appl. Phys. A* 76, 1025–1033 (2003).
- [12] A. Claverie, B. Colombeau, F. Cristiano, A. Altibelli, C. Bonafos. Modeling of the Ostwald ripening of extrinsic defects and transient enhanced diffusion in silicon, *Nucl. Instrum. Meth. Phys. Res. B* 186, 281–286 (2002).
- [13] I. Avci, M. E. Law, E. Kuryliw, A. F. Saavedra, K. S. Jones. Modeling extended defect ($\{311\}$ and dislocation) nucleation and evolution in silicon, *J. Appl. Phys.* 95, 2452-2460 (2004).
- [14] N. Zographos, C. Zechner, I. Avci. Efficient TCAD model for the evolution of interstitial clusters, $\{311\}$ defects, and dislocation loops in silicon, *Mat. Res. Soc. Symp. Proc.* 994, 297-306 (2007).
- [15] S. Lee, G. S. Hwang. Structure and stability of small compact self-interstitial clusters in crystalline silicon, *Phys. Rev. B* 77, 085210 (2008).
- [16] S. Lee, G. S. Hwang. Growth and shape transition of small silicon self-interstitial clusters, *Phys. Rev. B* 78, 045204 (2008).
- [17] S. S. Kapur, T. Sinno. Detailed microscopic analysis of self-interstitial aggregation in silicon. I. Direct molecular dynamics simulations of aggregation, *Phys. Rev. B* 82, 045205 (2010).
- [18] S. S. Kapur, A. M. Nieves, T. Sinno. Detailed microscopic analysis of self-interstitial aggregation in silicon. II. Thermodynamic analysis of single clusters, *Phys. Rev. B* 82, 045206 (2010).

- [19] S. Takeda, Structure analysis of defects in nanometer space inside a crystal: Creation and agglomeration of point defects in Si and Ge revealed by high-resolution electron microscopy, *Microsc. Res. Techniq.* 40, 313-335 (1998).
- [20] S. Boninelli, N. Cherkashin, A. Claverie, F. Cristiano. Evidences of an intermediate rodlike defect during the transformation of {113} defects into dislocation loops, *Appl. Phys. Lett.* 89, 161904 (2006).
- [21] H. Park, J. W. Wilkins. A topological point defect regulates the evolution of extended defects in irradiated silicon, *Appl. Phys. Lett.* 98, 171915 (2011).
- [22] C. Bonafos, D. Mathiot, A. Claverie. Ostwald ripening of end-of-range defects in silicon, *J. Appl. Phys.* 83, 3008-3017 (1998).
- [23] B. Rajendran, R. S. Shenoy, D. J. White, N. S. Chokshi, R. L. De Leon, G. S. Tompa, R. Fabian. Low thermal budget processing for sequential 3-D IC fabrication, *IEEE T. Electron. Dev.* 54, 707-714 (2007).
- [24] A. Vandooren , J. Franco, B. Parvais, Z. Wu, L. Witters , A. Walke, W. Li, L. Peng, V. Deshpande, F. M. Bufler, N. Rassoul, G. Hellings, G. Jamieson, F. Inoue, G. Verbinnen, K. Devriendt, L. Teugels, N. Heylen, E. Vecchio, T. Zheng, E. Rosseel, W. Vanherle, A. Hikavy, B. T. Chan, R. Ritzenthaler , G. Besnard, W. Schwarzenbach, G. Gaudin, I. Radu, B.-Y. Nguyen, N. Waldron, V. De Heyn, D. Mocuta, N. Collaert. 3-D sequential stacked planar devices featuring low-temperature replacement metal gate junctionless top devices with improved reliability, *IEEE Trans. Electron Dev.* 65, 5165-5171 (2018).
- [25] Y. Qiu, F. Cristiano, K. Huet, F. Mazzamuto, G. Fiscaro, A. La Magna, M. Quillec, N. Cherkashin, H. Wang, S. Duguay, D. C. Blavette. Extended defects formation in nanosecond laser-annealed ion implanted silicon, *Nano Lett.* 14, 1769-1775 (2014).

- [26] C. S. Rafferty, G. H. Gilmer, M. Jaraiz, D. Eaglesham, H.-J. Gossmann. Simulation of cluster evaporation and transient enhanced diffusion in silicon, *Appl. Phys. Lett.* 68, 2395-2397 (1996).
- [27] H. Bracht, E. E. Haller, R. Clark-Phelps. Silicon self-diffusion in isotope heterostructures, *Phys. Rev. Lett.* 81, 393-396 (1998).
- [28] L. A. Marqués, M. Aboy, I. Santos, P. López, F. Cristiano, A. La Magna, K. Huet, T. Tabata, L. Pelaz. On the anomalous generation of {001} loops during laser annealing of ion-implanted silicon, *Nuclear Inst. and Methods in Physics Research B*, <https://doi.org/10.1016/j.nimb.2018.09.030>.
- [29] L. A. Marqués, L. Pelaz, M. Aboy, I. Santos, P. López, F. Cristiano, A. LaMagna, K. Huet, T. Tabata, L. Pelaz. Ultrafast generation of unconventional {001} loops in Si, *Phys. Rev. Lett.* 119, 205503 (2017).
- [30] K. J. Dudeck, L. A. Marqués, A. P. Knights, R. M. Gwilliam, G. A. Botton. Sub-ångstrom experimental validation of molecular dynamics for predictive modeling of extended defect structures in Si, *Phys. Rev. Lett.* 110, 166102 (2013).
- [31] S. Plimpton. Fast parallel algorithms for short-range molecular dynamics, *J. Comp. Phys.* 117, 1-19 (1995).
- [32] J. Tersoff, Empirical interatomic potential for silicon with improved elastic properties, *Phys. Rev. B* 38, 9902-9905 (1988).
- [33] L. A. Marqués, L. Pelaz, M. Aboy, L. Enríquez, J. Barbolla. Microscopic description of the irradiation-induced amorphization in silicon, *Phys. Rev. Lett.* 91, 135504 (2003).
- [34] L. A. Marqués, L. Pelaz, J. Hernández, J. Barbolla, G. H. Gilmer. Stability of defects in crystalline silicon and their role in amorphization, *Phys. Rev. B* 64, 045214 (2001).

- [35] L. A. Marqués, L. Pelaz, P. Castrillo, J. Barbolla. Molecular dynamics study of the configurational and energetic properties of the silicon self-interstitial, *Phys. Rev. B* 71, 085204 (2005).
- [36] I. Santos, M. Aboy, L. A. Marqués, P. López, M. Ruiz, L. Pelaz, A. M. Hernández-Díaz, P. Castrillo. Atomistic study of the anisotropic interaction between extended and point defects in crystalline silicon and its influence on Si self-interstitial diffusion, *Proceedings of the 2016 International Conference on Simulation of Semiconductor Processes and Devices (SISPAD)*, Nuremberg, pp. 35-37 (2016).
- [37] S. K. Estreicher, M. Gharaibeh, P. A. Fedders, P. Ordejón. Unexpected dynamics for self-interstitial clusters in silicon, *Phys. Rev. Lett.* 86, 1247-1250 (2001).
- [38] I. Martin-Bragado, M. Jaraiz, P. Castrillo, R. Pinacho, J. Barbolla, M. M. De Souza. Mobile silicon di-interstitial: Surface, self-interstitial, and transient enhanced diffusion phenomena, *Phys. Rev. B* 68, 195204 (2003).
- [39] Atoms in perfect lattice positions, with S values between -0.5 and 0.5, are not shown. Atoms with positive S values are displayed with warm colors (from yellow to red), and atoms with negative S values are displayed with cold colors (from green to dark blue). In this way, it is possible to relate which regions are under compressive stress, and which ones are under tensile stress. Since excess \mathcal{S} -atoms generate strong compressive stress around them, defect cores are easily identified in the figures by atoms with dark blue colors.
- [40] L. Fedina, A. Gutakovskii, A. Aseev, J. Van Landuyt, J. Vanhellefont. On the mechanism of $\{111\}$ -defect formation in silicon studied by in situ electron irradiation in a high resolution electron microscope, *Phil. Mag. A* 77, 423-435 (1998).

- [41] N. Arai, S. Takeda, M. Kohyama. Self-interstitial clustering in crystalline silicon, *Phys. Rev. Lett.* 78, 4265-4268 (1997).
- [42] The full ripening process of the defects obtained at the end of the $T^* = 0.5$ annealing simulation cannot be directly simulated using MD techniques since involved time-scales are too large.
- [43] S. Birner, J. Kim, D. A. Richie, J. W. Wilkins, A. F. Voter, T. Lenosky. Accelerated dynamics simulations of interstitial-cluster growth, *Solid State Commun.* 120, 279-282 (2001).
- [44] Y. A. Du, R. G. Hennig, T. J. Lenosky, J. W. Wilkins. From compact point defects to extended structures in silicon, *Eur. Phys. J. B* 57, 229-234 (2007).
- [45] F. Cristiano, M. Shayesteh, R. Duffy, K. Huet, F. Mazzamuto, Y. Qiu, M. Quillec, H. H. Henrichsen, P. F. Nielsen, D. H. Petersen, A. LaMagna, G. Caruso, S. Boninelli. Defect evolution and dopant activation in laser annealed Si and Ge, *Mat. Sci. Semicon. Proc.* 42, 188–195 (2016).
- [46] S. S. Kapur, T. Sinno. Entropic origins of stability in silicon interstitial clusters, *Appl. Phys. Lett.* 93, 221911 (2008).
- [47] Some Arai tetra- \mathcal{S} s can be seen at the end of the annealing at $T^* = 0.79$, as shown in Fig.4(a). They also form during the \mathcal{S} aggregation process at $T^* = 0.83$ and $T^* = 0.88$, although they are not observed at the end of the annealing simulations because they are swept out by the moving liquid droplets.
- [48] L. A. Marqués, L. Pelaz, M. Aboy, J. Barbolla. The laser annealing induced phase transition in silicon: a molecular dynamics study. *Nucl. Instrum. Meth. Phys. Res. B* 216, 57-61 (2004).
- [49] Simulated HRTEM images have been obtained using the QSTEM software (https://www.physics.hu-berlin.de/en/sem/software/software_qstem) with a sample thickness

of 108 Å, voltage of 200 kV, defocus of 120 nm, and spherical aberration of 1 μm. Apart from the beam energy, the conditions in which the experimental image of ref. [25] was obtained were not reported. Consequently, we have chosen the previous parameters so that the contrast in the simulated image is similar to the one in the real image.